Supporting Information

Mandadapu et al. 10.1073/pnas.1501734112

SI Text

Model Equations

In *Materials and Methods*, we presented Langevin equations describing the dynamics of the two stator loops, the rotor, and the load. As described previously, the mechanics of the two stator loops are equivalent. Here, we provide a reduced model describing the dynamics of a stator with a single loop that generates torque both during bending (ϕ_S increasing) and unbending (ϕ_S decreasing). This model is isomorphic to the one described in the main text.

As described in *Mechanochemical Model* (and in ref. 5), the motion of the stator has two components: vertical and rotational. The vertical motion is necessary to describe partial power strokes and loose chemical coupling. The stator's ion-binding residue (Asp32) is very close to the cytoplasmic side of the membrane, and so the reaction coordinate for ion binding and release likely depends on both the stator's vertical z and rotational position ϕ_S.

Moreover, thermal fluctuations allow rapid movements of the Asp32 residue into the membrane and the cytoplasm, leading to an increased probability for the unbinding of ions before the power stroke is completed. This coupled reaction coordinate may also account for a reduction in the overall efficiency of the stator due to ion leakage. Furthermore, inclusion of the vertical motion of the stator allows consideration of the stator springs that connect MotB residues to the peptidoglycan layer of the bacterial cell wall (35, 36).

$$\textbf{Stator (rotation)}: \zeta_S \frac{d\phi_S}{dt} = \underbrace{K(z - f(\phi_S))}_{\substack{\text{Internal flexibility}\\ \text{of stator}}} - \underbrace{\frac{\partial G(\phi_S, j)}{\partial \phi_S}\ell_p}_{\substack{\text{Torque from}\\ \text{Proline hinge}}} - \underbrace{\frac{\partial V_{RS}}{\partial \phi_S}}_{\substack{\text{Reaction}\\ \text{from rotor}}} - \underbrace{\frac{\partial \psi}{\partial \phi_S}\ell_p}_{\substack{\text{Electrostatic}\\ \text{attraction}}} + \underbrace{\sqrt{2 k_B T \zeta_S} f_n(t)}_{\substack{\text{Thermal fluctuations}}} \quad \textbf{[S1]}$$

$$\textbf{Stator(vertical)}: \tilde{\zeta}_S \frac{dz_S}{dt} = - \underbrace{K(z - f(\phi_S))}_{\substack{\text{Internal flexibility}\\ \text{of stator}}} - \underbrace{k_s(z - z^0)}_{\substack{\text{Reaction}\\ \text{from rotor}}} + \underbrace{\sqrt{2 k_B T \tilde{\zeta}_S} f_n(t)}_{\substack{\text{Thermal fluctuations}}} \quad \textbf{[S2]}$$

$$\textbf{Rotor}: \zeta_R \frac{d\theta_R}{dt} = - \underbrace{\kappa(\theta_R - \theta_L)}_{\substack{\text{Spring connection}\\ \text{to load}}} - \underbrace{\frac{\partial V_{RS}}{\partial \theta_R}}_{\substack{\text{Torque}\\ \text{from stator}}} - \underbrace{\frac{\partial \psi}{\partial \theta_R} R}_{\substack{\text{Electrostatic}\\ \text{attraction}}} + \underbrace{\sqrt{2 k_B T \zeta_R} f_n(t)}_{\substack{\text{Thermal fluctuations}}} \quad \textbf{[S3]}$$

$$\textbf{Load}: \zeta_L \frac{d\theta_L}{dt} = \underbrace{\kappa(\theta_R - \theta_L)}_{\substack{\text{Spring connection}\\ \text{to rotor}}} + \underbrace{\sqrt{2 k_B T \zeta_L} f_n(t).}_{\substack{\text{Thermal fluctuations}}} \quad \textbf{[S4]}$$

Here, as before, ζ_S, ζ_R, and ζ_L are the effective rotational drag coefficients of the stator, rotor, and load; $\tilde{\zeta}_S$ is the linear drag coefficient of the stator. The last term in each equation is the stochastic Brownian force, where $f_n(t)$ is uncorrelated white noise. All other symbols are as described in Table 1. In writing the equations of motion, we assume that the stator rotates about the proline hinge. Similarly, the rotor rotates about the axis normal to the plane of the rotor and passing through its center.

In Eq. **S1**, the internal force driving the stator due to the rearrangement of hydrogen bonds caused by a proton-binding event is denoted by $F_p = \frac{\partial G}{\partial \phi_S}$. Here, $G(\phi_S, j)$ denotes the free energy of the stator. Due to the fact that thermal fluctuations are of a comparable magnitude to the free energies considered, the exact shape of the potentials is relatively unimportant. For ease of computation, we approximate the potential using a piecewise linear function. The exact mathematical formulation of these potentials is given in *Interaction Potentials*. In this setup, for a given proton motive force, the force applied on the rotor by the stator loop is constant and positive during each mechanical power stroke. At other times, there is little elastic strain on the MotA loops, and accordingly, the applied force is near zero.

Eq. **S2** governs the vertical motion of the MotB helix. The proposed kink-and-swivel motion of the MotA α-helices (see Fig. 3) may also shift the vertical position of the associated MotB helix. This collective motion would bring Asp32 residue into the cytoplasm during a power stroke. Here, K denotes the internal flexibility of the rotor and couples the motion of the proline-induced kink and swivel motion of MotA and the vertical motion of MotB helices. This coefficient is dependent on the hydrogen bonds between the MotA and MotB helices. For a perfect stator, the motion of the MotA and MotB helices are tightly coupled. The vertical motion of the stator complex is also determined by the stiffness coefficient k_S of the springs connecting the MotB helix to the peptidoglycan layer.

The torque generated by the stator is dependent on the applied load ζ_L as a natural consequence of steric forces. A general discussion on contact forces and the explicit formulation of the repulsive interaction potential V_{RS}, are provided in *Overview of Steric Forces* and *Rotor–stator interaction potential*, respectively. The contact torque applied to the rotor (in Eq. **S3**), and consequent reaction torque applied to the stator (in Eq. **S1**), are given by $\tau_{\text{contact}} = -\frac{\partial V_{RS}}{\partial \theta_R}$ and $\tau_{\text{reaction}} = -\frac{\partial V_{RS}}{\partial \phi_S}$.

Additionally, the charges on the FliG and the stator loop also exert weak attractive forces on each other. These forces prevent the drifting of the rotor with respect to the stator during the chemical transition events. Further discussion of these forces is included later in *Electrostatic Steering*. In the above equations, we denote this term via the term $-\frac{\partial\psi}{\partial\theta_R}R$; it detracts from the repulsive torque imposed by the steric force of the stator.

The rotor and load are connected by a linear spring with constant κ; the elastic coupling terms in the equations for the rotor and the load thus appear with opposite signs (in Eqs. **S3** and **S4**, respectively). The elastic constant in the experiments can vary depending on the length of the hook when attaching the bead. In some cases, the hook is very short or is stiffened by an antibody linker. This corresponds to a large spring coefficient (34). An analysis of this model in the corresponding limit $\kappa\to\infty$ is provided in *Approximation: Model Without Spring*.

For the computations in this manuscript, we have assumed that the stator is internally rigid—that is, the internal spring coefficient K is very large. This leads to a tightly coupled motion between the rotation and the vertical motion of the stator (i.e., $z=f(\phi_S)$), and allows us to ignore the thermal fluctuations and the effect of the peptidoglycan springs. A soft connection between the stator and the peptidoglycan layer was originally assumed to explain resurrection experiments showing that the zero-torque speed was independent of stator number (36). However, recent reports that these low-load experiments were likely performed on motors with a single stator (2) remove the need for the assumption of soft stator springs. Given this, we obtain the following reduced set of equations for the motion of the stator, rotor, and load:

$$\textbf{Stator}:\zeta_S\frac{d\phi_S}{dt}=-\underbrace{\frac{\partial G(\phi_S,j)}{\partial\phi_S}\ell_p}_{\substack{\text{Torque from}\\ \text{Proline hinge}}}-\underbrace{\frac{\partial V_{RS}}{\partial\phi_S}}_{\substack{\text{Reaction}\\ \text{from rotor}}}-\underbrace{\frac{\partial\psi}{\partial\phi_S}\ell_p}_{\substack{\text{Electrostatic}\\ \text{attraction}}}+\underbrace{\sqrt{2k_BT\zeta_S}f_n(t)}_{\text{Thermal fluctuations}} \quad \textbf{[S5]}$$

$$\textbf{Rotor}:\zeta_R\frac{d\theta_R}{dt}=-\underbrace{\frac{\partial V_{RS}}{\partial\theta_R}}_{\substack{\text{Torque}\\ \text{from stator}}}-\underbrace{\frac{\partial\psi}{\partial\theta_R}R}_{\substack{\text{Electrostatic}\\ \text{attraction}}}-\underbrace{\kappa(\theta_R-\theta_L)}_{\substack{\text{Spring connection}\\ \text{to load}}}+\underbrace{\sqrt{2k_BT\zeta_R}f_n(t)}_{\text{Thermal fluctuations}} \quad \textbf{[S6]}$$

$$\textbf{Load}:\zeta_L\frac{d\theta_L}{dt}=\underbrace{\kappa(\theta_R-\theta_L)}_{\substack{\text{Spring connection}\\ \text{to rotor}}}+\underbrace{\sqrt{2k_BT\zeta_L}f_n(t).}_{\text{Thermal fluctuations}} \quad \textbf{[S7]}$$

We use Eqs. **S5**–**S7** to obtain the majority of the results presented in the main text.

Simplified Deterministic Model

By taking an average over many trajectories, it is possible to generate a deterministic analog of the model presented above. Although numerical simulations on the full stochastic model were used for the results in this manuscript, the below formulation is convenient primarily for expository purposes. In particular, it admits explicit analytic solutions for many experimental situations. Before we provide the numerical implementation of the full Langevin equations (Eqs. **S5**–**S7**), we use the following model to introduce several important concepts.

The deterministic equations of motion can be obtained by time averaging Eqs. **S5**–**S7** as

$$\zeta_S\frac{d\phi_S}{dt}=F_p\ell_p-\frac{\langle\tau\rangle}{R}\ell_p \quad \textbf{[S8]}$$

$$\zeta_R\frac{d\theta_R}{dt}=\langle\tau\rangle-\kappa(\theta_R-\theta_L) \quad \textbf{[S9]}$$

$$\zeta_L\frac{d\theta_L}{dt}=\kappa(\theta_R-\theta_L). \quad \textbf{[S10]}$$

Note that in addition to time averaging, we have neglected the electrostatic term for computational convenience, as it tends to be quite small in value. Here, the average torque on the rotor $\langle\tau\rangle$ results from averaging the torque on the rotor as $\tau_{\text{contact}}=-\partial V_{RS}/\partial\theta_R$ over many trajectories. The return force then can be calculated by $\langle\tau\rangle/R$, which is then multiplied by ℓ_p to calculate the return torque. The internal torque of the proline hinge for a given IMF is $F_p\ell_p=-\frac{\partial G}{\partial\phi_S}\propto\text{IMF}$. The averaged equations do not contain a noise term because the terms $f_n(t)$ are Gaussian with mean zero. In the following, we compute expressions for the average torque and speed during a single power stroke of the motor from the above deterministic model.

Under the assumption that all active stators act in synchrony, Eq. **S8** can be generalized to a motor with N stators as follows. An analog of Eq. **S8** now corresponds to the motion of the ith stator ($i\in 1,2,\ldots N$),

$$\zeta_S\frac{d\phi_S^i}{dt}=F_p\ell_p-\frac{\langle\tau_i\rangle}{R}\ell_p,\quad i\in 1,2,\ldots,N. \quad \textbf{[S11]}$$

We then can sum the equations of all stators, which results in

$$N\zeta_S\frac{d\phi_S^i}{dt}=NF_p\ell_p-\frac{\langle\tau\rangle}{R}\ell_p. \quad \textbf{[S12]}$$

Note that we have used the fact that $N\langle\tau_i\rangle=\langle\tau\rangle$. Similarly, an equation for the rotor in a motor with multiple stators can be written as

$$\zeta_R\frac{d\theta_R}{dt}=\sum_{i=1}^{N}\langle\tau^i\rangle-\kappa(\theta_R-\theta_L)=\langle\tau\rangle-\kappa(\theta_R-\theta_L), \quad \textbf{[S13]}$$

which is the same form as Eq. **S9**. Note that only the terms corresponding to the stators are summed (i.e., the connection term between the rotor and the load is not multiplied by N). Eq. **S10** also remains as for the single-stator case because the spring connection term is unaffected by the addition of torque-generating units.

The three equations of motion, Eqs. **S8**–**S10**, for a single stator contain four unknowns $\{\theta_R,\theta_L,\phi_S,\langle\tau\rangle\}$. This results in an indeterminate system, and requires the addition of an equation to generate a unique solution. This additional equation can be obtained from a fundamental property of contact forces. Because the stator loop is in contact with the rotor during the power stroke, the velocities of the stator loop and the rotor must be equal. This leads to a contact condition for the tangential velocities of the stator loop and the rotor,

$$\boxed{\ell_p\frac{d\phi_S}{dt}=R\frac{d\theta_R}{dt}.} \quad \textbf{[S14]}$$

Analysis. Multiplying Eq. **S12** by R/ℓ_p and summing with Eq. **S9** gives

$$\frac{NR\zeta_S}{\ell_p}\frac{d\phi_S}{dt}+\zeta_R\frac{d\theta_R}{dt}=NF_pR-\kappa(\theta_R-\theta_L). \quad \textbf{[S15]}$$

Rearranging Eq. **S14**, we get

$$\frac{d\phi_S}{dt}=\frac{R}{\ell_p}\frac{d\theta_R}{dt}. \quad \textbf{[S16]}$$

Substituting into Eq. **S15**,

$$\begin{aligned}\frac{NR^2\zeta_S}{\ell_p^2}\frac{d\theta_R}{dt}+\zeta_R\frac{d\theta_R}{dt}&=NF_pR-\kappa(\theta_R-\theta_L)\\ \zeta_R\frac{d\theta_R}{dt}\left(\frac{NR^2\zeta_S}{\ell_p^2\zeta_R}+1\right)&=NF_pR-\kappa(\theta_R-\theta_L)\\ \zeta_R\frac{d\theta_R}{dt}(NM+1)&=NF_pR-\kappa(\theta_R-\theta_L),\end{aligned} \quad \textbf{[S17]}$$

where $M=(R^2\zeta_S)/(\ell_p^2\zeta_R)$. Rewriting Eq. **S17** gives us

$$\frac{d\theta_R}{dt}=\frac{NF_pR}{\zeta_R(NM+1)}-\frac{\kappa}{\zeta_R(NM+1)}(\theta_R-\theta_L). \quad \textbf{[S18]}$$

Dividing Eq. **S10** by ζ_L and subtracting Eq. **S18** leads to

$$\frac{d(\theta_R-\theta_L)}{dt}=\frac{F_pR}{\zeta_R(NM+1)}-\kappa\left(\frac{1}{\zeta_R(NM+1)}+\frac{1}{\zeta_L}\right)(\theta_R-\theta_L). \quad \textbf{[S19]}$$

This differential equation has the solution

$$\boxed{(\theta_R-\theta_L)(t)=\frac{A^*\left(1-e^{-\alpha^*t}\right)}{\alpha^*},} \quad \textbf{[S20]}$$

where $A^*:=F_pR/[\zeta_R(NM+1)]$ and $\alpha^*:=\kappa([1/\zeta_R(NM+1)]+(1/\zeta_L))$.

Substituting expressions for $d\phi_S/dt$ and $d\theta_R/dt$ from Eqs. **S12** and **S9**, respectively, into the equation for contact condition (Eq. **S14**) leads to

$$\frac{\ell_p^2}{N\zeta_S}\left(NF_pR-\tau\right)=\frac{R^2}{\zeta_R}\left[\tau-\kappa(\theta_R-\theta_L)\right]. \qquad \textbf{[S21]}$$

Note that, because we are interested in the full time course, we consider $\tau=\tau(t)$ rather than the average torque $\langle\tau\rangle$. Rearranging and solving for τ,

$$\tau=\frac{N\zeta_R R\left[F_p\ell_p^2-\zeta_S R\kappa(\theta_R-\theta_L)\right]}{\zeta_R\ell_p^2+N\zeta_S R^2}. \qquad \textbf{[S22]}$$

Plugging in the derived expression for $(\theta_R-\theta_L)$ from Eq. **S20**,

$$\tau=\frac{F_p\ell_p^2 NR\zeta_R\zeta_S\left[\frac{1}{\zeta_S}+\frac{\left(1-\exp\left[\kappa t\left(\frac{1}{\zeta_L}+\frac{1}{\zeta_R+NR^2\zeta_S/\ell_p^2}\right)\right]\right)NR^2\zeta_S}{\zeta_R\left(\ell_p^2(\zeta_L+\zeta_R)+NR^2\zeta_S\right)}\right]}{\ell_p^2\zeta_R+NR^2\zeta_S}. \qquad \textbf{[S23]}$$

From this value, we can calculate the average torque in a single step $\langle\tau\rangle$ by

$$\boxed{\langle\tau\rangle=\frac{1}{T_m}\int_0^{T_m}\tau(t)dt=\frac{F_p\ell_p^2NR\left(\left(-1+\exp\left[\kappa T_m\left(-\frac{1}{\zeta_L}-\frac{1}{\zeta_R+NR^2\zeta_S/\ell_p^2}\right)\right]\right)NR^2\zeta_L^2\zeta_S+\kappa T_m(\zeta_L+\zeta_R)\left(\ell_p^2(\zeta_L+\zeta_R)+NR^2\zeta_S\right)\right)}{\kappa T_m\left(\ell_p^2(\zeta_L+\zeta_R)+NR^2\zeta_S\right)^2}} \qquad \textbf{[S24]}$$

where T_m is the time spent moving during a step. Likewise, we can also calculate the speed of the load $d\theta_L/dt$ from Eqs. **S10** and **S20**,

$$\frac{d\theta_L}{dt}=\frac{1}{\zeta_L}\kappa(\theta_R-\theta_L)=\frac{\left(1-\exp\left[-\kappa t\left(\frac{1}{\zeta_L}+\frac{1}{\zeta_R+NR^2\zeta_S/\ell_p^2}\right)\right]\right)F_p\ell_p^2NR}{\ell_p^2(\zeta_L+\zeta_R)+NR^2\zeta_S}. \qquad \textbf{[S25]}$$

As with torque, we integrate over a time step to find the average speed $\langle d\theta_L/dt\rangle$,

$$\boxed{\left\langle\frac{d\theta_L}{dt}\right\rangle=\frac{F_p\ell_p^2NR\left[\left(-1+\exp\left[\kappa T_m\left(-\frac{1}{\zeta_L}-\frac{1}{\zeta_R+NR^2\zeta_S/\ell_p^2}\right)\right]\right)\zeta_L\left(\ell_p^2\zeta_R+NR^2\zeta_S\right)+\kappa T_m\left(L^2(\zeta_L+\zeta_R)+NR^2\zeta_S\right)\right]}{\kappa T_m\left(\ell_p^2(\zeta_L+\zeta_R)+NR^2\zeta_S\right)^2}} \qquad \textbf{[S26]}$$

Using Eqs. **S24** and **S26**, we can calculate a family of parametric torque–speed curves (parametrized by the load ζ_L), where each curve corresponds to a motor with a constant number of synchronously stepping stators. Computed curves for motors with 1,2, . . . , 7 stators are shown in Fig. S4.

Approximation: Model Without Spring. In most experimental setups, the filament is removed and a bead is attached to a shortened hook connection. Additionally, the hook is sometimes stiffened with an antibody linker. These setups have a rigid connection between the rotor and the load, corresponding to a large spring constant. In this section, we perform a similar analysis to that in *Analysis* for the limit $\kappa\to\infty$. The calculations performed in this section provide analytic formulas for a clear physical understanding of several important properties of the model.

The rotation rates of the rotor and load become equal after an initial wind-up period. That is, the rotor and load move at the same angular speed (i.e., $d\theta_R/dt=d\theta_L/dt$) after the system reaches a steady state. Note, however, that the angular positions θ_R and θ_L still maintain a (constant) offset. This can be seen explicitly by subtracting Eqs. **S9** and **S10**,

$$\begin{aligned}\frac{d\theta_R}{dt}-\frac{d\theta_L}{dt}&=\frac{\langle\tau\rangle}{\zeta_R}-\kappa\left(\frac{1}{\zeta_R}+\frac{1}{\zeta_L}\right)(\theta_R-\theta_L)\\ \frac{d(\theta_R-\theta_L)}{dt}&=\frac{\langle\tau\rangle}{\zeta_R}-\kappa\left(\frac{1}{\zeta_R}+\frac{1}{\zeta_L}\right)(\theta_R-\theta_L).\end{aligned} \qquad \textbf{[S27]}$$

To simplify some notation, we define $x:=(\theta_R-\theta_L)$, $\alpha:=\kappa[(1/\zeta_R)+(1/\zeta_L)]$ and $A:=\langle\tau\rangle/\zeta_R$, and rewrite Eq. **S27**,

$$\frac{dx}{dt}=A-\alpha x. \qquad \textbf{[S28]}$$

As in *Analysis*, we can solve for the time course $x(t) = (\theta_R - \theta_L)(t)$,

$$\boxed{x(t) = (\theta_R - \theta_L)(t) = \frac{A(1 - e^{-\alpha t})}{\alpha}.} \quad \textbf{[S29]}$$

By definition, $\alpha > 0$, and so it is clear that $x(t)$ will reach a constant value after an initial startup. As $\kappa \to \infty$, the wind-up time goes to zero and $d\theta_R/dt = d\theta_L/dt$ in this limit.

Summing Eqs. **S9** and **S10** gives us

$$\zeta_R \frac{d\theta_R}{dt} + \zeta_L \frac{d\theta_L}{dt} = \langle \tau \rangle. \quad \textbf{[S30]}$$

We approximate $\frac{d\theta_R}{dt} = \frac{d\theta_L}{dt}$ when κ is large, and Eq. **S30** reduces to

$$(\zeta_R + \zeta_L) \frac{d\theta_R}{dt} = \langle \tau \rangle. \quad \textbf{[S31]}$$

We multiply Eqs. **S12** and **S31** by ℓ_p and R, respectively. After some algebra,

$$\ell_p \frac{d\phi_S}{dt} = \frac{\ell_p^2}{N\zeta_S} \left(NF_p - \frac{\langle \tau \rangle}{R} \right) \quad \textbf{[S32]}$$

$$R \frac{d\theta_R}{dt} = \frac{R\langle \tau \rangle}{(\zeta_L + \zeta_R)}. \quad \textbf{[S33]}$$

Given the relationship S14, we equate the two right-hand sides of Eqs. **S32** and **S33**,

$$\begin{aligned} \frac{\ell_p^2}{N\zeta_S} \left(NF_p - \frac{\langle \tau \rangle}{R} \right) &= \frac{R\langle \tau \rangle}{(\zeta_L + \zeta_R)} \\ \frac{\ell_p^2 R}{\zeta_S} \left(NF_p R - \langle \tau \rangle \right) &= \frac{NR^2 \langle \tau \rangle}{(\zeta_L + \zeta_R)}. \end{aligned} \quad \textbf{[S34]}$$

Here, the second line is obtained simply by multiplying through by N and R. Solving for $\langle \tau \rangle$,

$$\boxed{\langle \tau \rangle = \frac{NF_p R}{\left(1 + \frac{NR^2 \zeta_S}{(\zeta_L + \zeta_R)\ell_p^2} \right)}.} \quad \textbf{[S35]}$$

We can use this expression to attempt some intuition for the result of Sowa et al. (16) regarding torque and stator number at high and low loads. Consider the following two limits of Eq. **S35**: (*i*) high load, when $\zeta_L \gg \zeta_R$, and (*ii*) low load, where $\zeta_L \ll \zeta_R$.

In the first case, we have

$$\langle \tau \rangle_{\text{high}} = \frac{NF_p R}{\left(1 + \frac{NR^2 \zeta_S}{(\zeta_L + \zeta_R)\ell_p^2} \right)} \approx \frac{NF_p R}{\left(1 + \frac{NR^2 \zeta_S}{\zeta_L \ell_p^2} \right)} \approx NF_p R. \quad \textbf{[S36]}$$

The third line follows from the fact that $\zeta_S < \zeta_R \ll \zeta_L$. For very high loads, the observed torque is 180 pN·nm, and therefore the force $F_p \approx 9.5$ pN. Eq. **S36** suggests that the torque increases linearly with stator number under extremely large loads as observed in the experiments. However, for a given ζ_L, it can be seen that nonlinearities can arise in the torque versus number of stators even in the high load limit. This property is primarily due to the nature of contact forces, and is not applicable to previous models that assume constant torque between stator and rotor.

Conversely, at low loads ($\zeta_L/\zeta_R \ll 1$),

$$\langle \tau \rangle_{\text{low}} = \frac{NF_p R}{\left(1 + \frac{NR^2 \zeta_S}{(\zeta_L + \zeta_R)\ell_p^2} \right)} \approx \frac{NF_p R}{\left(1 + \frac{NR^2 \zeta_S}{\zeta_R \ell_p^2} \right)}. \quad \textbf{[S37]}$$

The torque measured at high speeds is ~20 pN·nm (3). Then, from Eq. **S37**, the nondimensional number $NR^2\zeta_S/\zeta_R\ell_p^2 \approx 10$. Also, Eq. **S37** shows that the torque and speed are not linearly dependent on the number of stators at low loads. This is consistent with previous experimental observations (35).

The above approximations to the full model are primarily laid out for expository purposes, to introduce general properties of the model. As such, there are several limitations due to the assumptions made, which we outline below.

Firstly, the observations from Sowa et al. are under question given that motors with more than one (or a few) stator may not have been considered in low-load measurements. To determine whether the stators do indeed act independently or in synchrony, experiments that directly account for the number of active stators must be performed. The extension of our model to N stators is dependent on the assumption that all stators step in synchrony, and the above results will not hold if stators are independent stochastic steppers. Because of the recent measurements made on single-stator motors, we have chosen to largely focus on the explicit modeling of the intrinsic mechanism of torque generation in the BFM rather than on the potential interaction between stators. Although a thorough exploration of the dynamics of multiple-stator motors is extremely worthwhile, it is out of the scope of the current paper.

There are also some inconsistencies in the approximation of an infinitely stiff spring at intermediate and low loads when the motor is not in the mechanically limited regime. We have that $\ell_p \approx 7$ nm, $R \approx 20$ nm, and the nondimensional number $NR^2\zeta_S/\zeta_R\ell_p^2 \approx 10$ at low loads. Then, from Eq. **S37**, the ratio of the stator and rotor drags $\zeta_S/\zeta_R \approx 1$. Using this, we can estimate the viscosities of the stator and rotor. The drag of the rotor is given by

$$\zeta_R = \frac{32}{3}\eta_R R^3, \qquad \textbf{[S38]}$$

where η_R is the viscosity of the rotor. An estimate for the drag coefficient of the stator can be obtained by using Eq. **S31** and the maximum observed speed of the wild-type motor (200 Hz), yielding $\zeta_S = 0.017$ pN·nm·s·rad^{-1}. Because the drag ratio of the stator and rotor is approximately unity, $\zeta_R \approx 0.017$ pN·nm·s·rad^{-1}. Using Eq. **S38**, the viscosity of the rotor is ∼2 poise. This is consistent with the fact that the cytoplasm is a mixture of water and proteins (1).

Likewise, the drag coefficient of the stator loop with a lever arm of length ℓ_p is given by

$$\zeta_S = \frac{\pi}{3}\frac{\eta_S\ell_p^3}{\log\left(\frac{\ell_p}{R_p}\right) - 0.66}, \qquad \textbf{[S39]}$$

where η_S is the viscosity of the stator and R_p is the radius of the stator loop. Then, using Eq. **S39** and a length to width ratio $\ell_p/R_p \approx 10$, we estimate the viscosity of the stator to be 800 poise. This value is three orders of magnitude higher than the viscosity of a regular lipid membrane and two orders of magnitude higher than the viscosity of a biological membrane. As this calculation of stator drag arises from estimates of limiting speed, it ignores the contribution of the kinetics of ion movement, particularly the diffusion-limited arrival at the channel (T_W). The discrepancy between this estimated drag coefficient and biologically reasonable values highlights the importance of the inclusion of chemical kinetics in the model, which are detailed in *Addition of Chemical Kinetics*.

Moreover, the torque–speed curves produced by the stiff-spring approximation are linear, in contrast to the concave-down torque speed curves observed in single-stator motors (3). Because the IMF enters only through the dependence of the torque, the speed–IMF curves are also linear at all loads, again in contrast to the recent 100-nm bead experiments on a single stator (3).

Addition of Chemical Kinetics. The linear torque–speed curves of a mechanically rate-limiting model elucidate the importance of the inclusion of ion-binding kinetics. In this case, these are events related to the binding of a cation from the periplasm to Asp32 and the unbinding of the cation from Asp32 into the cytoplasm. In this section, we recompute model torque–speed curves explicitly including the dwell times corresponding to the ion-binding and unbinding events between the power strokes.

As done by Meacci and Tu (8), a torque generation cycle is divided into two parts: (*i*) moving time T_m and (*ii*) waiting time T_w. Assuming that the ions bind only when the stators are around the minimum of the respective free-energy potentials, we may use the above model during T_m and sample T_w from an exponential distribution at the end of each moving step.

In a motor with a single stator ($N = 1$), the instantaneous torque is obtained from Eq. **S35** as

$$\tau = \frac{F_p R}{\left(1 + \frac{R^2\zeta_S}{(\zeta_L + \zeta_R)\ell_p^2}\right)}. \qquad \textbf{[S40]}$$

The force applied by the proline hinge is given as $F_p = -(\Delta G/\Delta\phi) = -(2q\ \text{IMF}/\Delta\phi)$, where q is the charge of the ion. The time required to move an angular distance of $2\pi/26$ in step i can be calculated from Eq. **S40** through the relationship $\omega = \tau/(\zeta_R + \zeta_L)$.

$$T_m^i = T_m = \frac{2\pi}{26}(\zeta_R + \zeta_L)\left(1 + \frac{R^2\zeta_S}{(\zeta_L + \zeta_R)\ell_p^2}\right)\frac{1}{F_p R}. \qquad \textbf{[S41]}$$

Let T_w^i be the waiting time that follows step i. During the waiting time, the instantaneous torque is zero. When the system reaches the steady state, the average torque $\langle\tau\rangle$ can be obtained via a time average

$$\langle\tau\rangle = \lim_{T\to\infty}\frac{1}{T}\int_0^T \tau(t')t', \qquad \textbf{[S42]}$$

where T is large. If there are N steps in time T, then there are N waiting times. Therefore, Eq. **S42** can be approximated as

$$\langle\tau\rangle = \lim_{T\to\infty}\frac{1}{T}\int_0^T \tau(t')t' \approx \frac{\sum_{i=1}^N \tau T_m}{T} = \frac{\sum_{i=1}^N \tau T_m}{\sum_{i=1}^N T_m^i + \sum_{i=1}^N T_w^i} = \frac{\tau T_m}{T_m + \frac{1}{N}\sum_{i=1}^N T_w^i}. \qquad \textbf{[S43]}$$

The average dwell time $(1/N)\sum_{i=1}^{N} T_w^i$ can be approximated as $\langle T_w \rangle = [k_0 \exp(\mathrm{IMF}/\mathrm{k_B T})]^{-1}$, where k_0 is a proportionality constant related to the rate of hopping of the ions. Using this, Eq. **S43** reduces to

$$\langle \tau \rangle = \frac{\tau T_m}{T_m + \langle T_w \rangle}. \quad \textbf{[S44]}$$

Likewise, the speed of the rotor (or the bead in the large spring constant limit) can be written as a time average

$$\left\langle \frac{d\theta_R}{dt} \right\rangle \approx \lim_{T\to\infty} \frac{1}{T} \int_0^T \frac{\theta_R(t')}{t'} t' = \frac{\frac{2\pi}{26T_m} T_m}{T_m + \frac{1}{N}\sum_{i=1}^{N} T_w^i} = \frac{\frac{2\pi}{26T_m} T_m}{T_m + \langle T_w \rangle} \quad \textbf{[S45]}$$

where the instantaneous speed is $(2\pi/26) \times (1/T_m)$ during the power stroke and zero during the dwell time.

The torque during a power stroke τ, the time taken by a single step T_m, and the dwell time T_w all depend on the IMF. Thus, Eqs. **S43** and **S45** point to the existence of nonlinearity in the torque–speed and speed–proton motive force (PMF) curves. These curves are presented and explained in *Results and Predictions*.

Overview of Steric Forces

In this section, we describe our modeling of the steric forces between the stator and the rotor, as well as a general discussion on the nature of contact/steric forces in a low Reynolds number environment. The behavior of objects moving at low Reynolds number is counterintuitive. When the Reynolds number is small, viscous forces dominate over inertial forces and inertia can be ignored (32). In the following, we illustrate some of these properties using a simple linear momentum balance. We can then extend this analysis to angular momentum balances, which are directly relevant to the BFM.

Consider a force F pushing an object A that is in contact with a larger object, B, as shown in Fig. S3. We denote the drag coefficients on objects A and B as ζ_A and ζ_B, respectively. Let us consider the following two situations.

Case 1. For Case 1, if F is applied to A, how much force is transferred to B when they are in contact, as shown in Fig. S3*A*? The corresponding free-body diagrams for A and B are shown in Fig. S3*B*; in the steady state, the force balances can be written as

$$\begin{aligned} F - F_c - \zeta_A v_A &= 0 \\ F_c - \zeta_A v_A &= 0. \end{aligned} \quad \textbf{[S46]}$$

In Eq. **S46**, v_A and v_B are the velocities of objects A and B, respectively, and F_c is the contact force between objects A and B. When the two objects are in contact and are moving together, the following contact condition ensures that the velocity of the objects are equal:

$$v_A = v_B. \quad \textbf{[S47]}$$

In this case, the force transferred by A to B (the contact force, F_c) is obtained by solving Eq. **S46**,

$$F_c = \frac{F}{1 + \zeta_A/\zeta_B}. \quad \textbf{[S48]}$$

When the drag on B is large, i.e., $\zeta_A/\zeta_B \ll 1$, almost all of force F is transferred to object B. Conversely, when $\zeta_A/\zeta_B \gg 1$, then most of the force is consumed to drag object A with little force transferred to object B.

Case 2. Case 2 is when there are N objects of type A in contact with B, each with a force F applied to them. This case is shown in Fig. S3*C*. As in the first case, we are concerned with how much of F is transferred to B. Again, using free-body diagrams (shown in Fig. S3*D*), we can write the equations of motion for the objects as

$$\begin{aligned} F - F_c^i - \zeta_A v_A^i &= 0 \quad i \in \{1, \ldots, N\}, \\ \sum_{i=1}^{N} F_c^i - \zeta_B v_B &= 0, \end{aligned} \quad \textbf{[S49]}$$

where F_c^i is the contact force between the ith object of type A and object B. As before, when the objects are in contact, the contact condition ensures that $v_A^i = v_B$ for all i. Therefore, the force transferred to B by N objects of type A can be derived from Eq. **S49** as

$$F_c = \sum_{i=1}^{B} F_c^i = \frac{NF}{1 + N\zeta_A/\zeta_B}. \quad \textbf{[S50]}$$

When $\zeta_A/\zeta_B \ll 1$, $F_c \approx NF$. Therefore, the force transferred is multiplied by the number of objects pushing B. However, when $\zeta_A/\zeta_B \gg 1$, then the force transferred is $F_c \approx F/(\zeta_A/\zeta_B) \approx 0$. Finally, when $\zeta_A/\zeta_B \approx 1$, then the force transferred is $F_c \approx F$ (i.e., the force transferred in this system is approximately the same as a single object A pushing B).

The above properties of contact forces can be applied to the BFM by identifying object A as the stator and B as the rotor–load system (i.e., the rotor and the bead), and F as the internal force generated by the proline hinge pushing the stator from its straight to bent state.

For large loads (e.g., large beads), almost all of the force generated by the stator is transferred to the rotor; i.e., the torque is close to stall. Moreover, as more stators are recruited, the force transferred increases linearly with the number of active stators, in accordance with the observed linear speed dependence on the number of stators near stall torque. By contrast, at zero load, if there exists a situation where the stator and rotor drags are comparable, then the above analysis suggests that the force transferred during a single step is equivalent to a single stator pushing the rotor. This suggests that, if the assumption that stators step in synchrony holds, torque and speed at low loads may be independent of the number of active stators.

In addition to the above, contact forces also have the following important implications for the BFM: (*i*) Because it operates at low Reynolds number, the rotor moves only as long as it is pushed by the stator. This assures that the rotor never moves faster than the stator. (*ii*) Experiments based on torque–speed curves alone may never be able to detect the number of operating stators at different loads (e.g., if both torque and speed are independent of the number of stators at low load). Rather, one likely needs chemical markers such as GFP tags as used in ref. 31 to identify the number of docked and engaged stators for a given load. (*iii*) The torque generated by the BFM depends on the bead size and is not constant across applied loads, as it was considered to be by previous models (7–9).

Interestingly, the speed of the BFM has been shown to be slightly nonlinearly dependent on the number of stators at high loads (Fig. S4). A linear relationship between speed and stator number would imply (*i*) that the applied force of the stator is independent of the load and (*ii*) that all stators act independently. Our results suggest that this nonlinearity may arise as a natural consequence of the steric force in (at least partially) coupled stators. Further experiments will be needed to further explore this hypothesis.

Numerical Implementation

In *Model Equations, Simplified Deterministic Model, Approximation: Model without Spring*, and *Addition of Chemical Kinetics*, we have provided the equations of our model, as well as analytic solutions for reduced deterministic approximations. In this section, we provide details on numerical implementation of the full stochastic model, using several arguments from our discussion on steric forces.

Interaction Potentials. In this section, we provide explicit forms of the free-energy potentials in terms of the order parameters we choose to describe the motion of the stator and the rotor.

Stator potentials. The order parameter describing the motion of the stator is the angle subtended by the stator loops $\phi_S^{1,3}$ with respect to the vertical MotB ion channels. When two ions bind to the Asp32 residues, the two loops undergo a conformational change from their straight ($\phi_S^{1,3}=0°$) to bent state ($\phi_S^{1,3}=20°$). In this work, we have assumed that the stator loops move in phase. Therefore, as previously, we model the two-stator loop configurations using a single collective parameter ϕ_S.

Before the ions bind to the Asp32 residues, the motion of the stators is governed by the potential $G_1(\phi_S)$, where the minimum is around $\phi_S=0°$, as shown in Fig. S5. When two ions bind to two Asp32s, the stator potential switches from G_1 to G_2. This compels the stator angle to move from $\phi_S=0°$ to $\phi_S=20°$.

During this transformation, the loop pushes the rotor via a steric force. At the end of the conformational change, when the loops are at the minimum of the potential G_2, the two ions bound to two Asp32s exit into the cytoplasm. The potential then switches back from to G_1, and the loops traverse back to $\phi_S=0°$. During this time, the loops apply a contact force on the same FliG as in the previous substep.

As noted previously, thermal fluctuations are of the same order of magnitude as the free energies considered, and the precise form of the potentials is not important. In our simulations, we choose

$$G_1(\phi)=\begin{cases}\beta\phi^2 & \text{if } \phi\le 0\\ F_p\phi & \text{if } 0\le\phi\le\phi_{max}\\ F_p\phi_{max}+\beta(\phi-\phi_{max})^2 & \text{if } \phi\ge\phi_{max}\end{cases}$$

and

$$G_2(\phi)=\begin{cases}\beta\phi^2 & \text{if } \phi\le 0\\ -F_p(\phi) & \text{if } 0\le\phi\le\phi_{max}\\ -F_p\phi_{max}+\beta(\phi-\phi_{max})^2 & \text{if } \phi\ge\phi_{max}.\end{cases}$$

Rotor–stator interaction potential. The steric force between the stator and the rotor can be simulated using a soft linear repulsive force with a cutoff distance X_{RS}.

$$V_{RS}(\phi_S^i,\theta_R)=\begin{cases}-F_{RS}\dfrac{(R\theta_R-\ell_P\phi_S)^2}{X_{RS}} & \text{if } 0\le x\le X_{RS}\\ 0 & \text{otherwise.}\end{cases}$$

The torque on the rotor can be obtained as $\tau_{\text{contact}}=-\partial V_{RS}/\partial\theta_R$,

$$\tau_{\text{contact}}(x)=\begin{cases}-F_{RS}R\dfrac{R\theta_R-\ell_P\phi_S}{X_{RS}}=F_{RS}R\left(1-\dfrac{x_{RS}}{X_{RS}}\right) & \text{if } 0\le x_{RS}\le X_{RS}\\ 0 & \text{otherwise.}\end{cases}$$

Likewise, the reaction torque on the stator is $-(\partial V_{RS}/\partial\phi_S)$. F_{RS} is the maximum force that can be applied by the proline hinge, and $x_{RS}=X_{RS}+R\theta_R-\ell_P\phi_S$ denotes the distance between the position of the stator loop and the nearest FliG (see Fig. S6). All other parameters are defined as described previously.

Note that we assume that weak electrostatic forces place the stator at most 0.5 nm from the nearest FliG on the rotor ($X_{RS} \approx 0.5$ nm) before the start of the power stroke, as shown in Fig. S6. During the half-step, the stator moves from $\phi_S = 0°$ to $\phi_S = 20°$. In this process, a contact force is applied on the rotor when $0 \le x_{RS} \le X_{RS}$. The contact force is zero when $x_{RS} \ge X_{RS}$.

All previous theoretical studies of the BFM have chosen to model the interactions between the stator and the rotor as a load-independent force. In *Simplified Deterministic Model*, we have shown that the dependence of steric forces on the load reproduces many of the mechanical characteristic features of the motor found in experiments (e.g., the nonlinearities in the relationship between speed and stator number at high loads).

Although the exact form of the potential used to model the rotor–stator interaction is not very important, we note that linear potentials cannot be used. Such potentials result in a constant torque, independent of ζ_L, and thus do not reproduce several properties of steric forces.

Kinetics of Ion Binding. In this section, we will describe how to model ion-binding events as part of the Langevin equation framework. In many problems related to motors, the ion-binding events may occur only in a certain window of a continuous coordinate describing the mechanical motion of the system. In the BFM, there are two main ion-binding events involved in the torque generation cycle.

i) Two cations (here, protons) from the periplasm bind to the Asp32 residue on two MotBs or unbind into the cytoplasm when the cytoplasmic loops are straight.

$$\mathrm{Asp32^- + H^+_{periplasm} \underset{k_{21}}{\overset{k_{12}}{\rightleftharpoons}} Asp32 - H.} \quad \textbf{[S51]}$$

ii) Once the protons are bound, the cytoplasmic loops undergo conformational change from the straight state into the bent state. At the end of the conformational process, the two channels close with respect to the periplasm and instead open toward the cytoplasm. Once this occurs, the two protons unbind from Asp32 residues into the cytoplasm (or, in the reverse reaction, bind from cytoplasm to Asp32).

$$\mathrm{Asp32 - H \underset{\tilde{k}_{21}}{\overset{\tilde{k}_{12}}{\rightleftarrows}} Asp32^- + H^+_{cytoplasm}.} \quad \textbf{[S52]}$$

First, we will describe the case for the kinetics at equilibrium (i.e., at zero IMF), followed by the procedure to model the kinetics under a nonzero IMF.

Equilibrium kinetics under zero IMF. In the following, we consider the proton-driven motor of *E. coli*, and so the IMF concerned is the PMF. When there is no PMF, the forward and backward reaction rates for the reaction in Eq. **S51** must satisfy

$$\frac{k_{12}}{k_{21}} = \frac{[\mathrm{Asp32 - H}]}{[\mathrm{Asp32}]}. \quad \textbf{[S53]}$$

Let the equilibrium dissociation constant of reaction **S51** be defined as

$$\mathrm{K_a^p} = \frac{[\mathrm{Asp32}]\left[\mathrm{H^+_{periplasm}}\right]}{[\mathrm{Asp32 - H}]}. \quad \textbf{[S54]}$$

If $\mathrm{pK_a^p} = -\log_{10}\mathrm{K_a^p}$, then the forward and backward rates should satisfy

$$\frac{k_{12}}{k_{21}} = 10^{\left(\mathrm{pK_a^p - pH_{periplasm}}\right)}. \quad \textbf{[S55]}$$

Note that the acid dissociation constant value of $\mathrm{pK_a^p}$ should be determined from experiments. A similar relation to the above can be derived for the reaction in Eq. **S52**.

Kinetics under nonzero IMF. To satisfy detailed balance when the PMF is nonzero, the kinetic coefficients for the reaction should satisfy

$$\frac{k_{12}}{k_{21}} = 10^{\left(\mathrm{pK_a^p - pH_{periplasm}}\right)} \exp\left(\frac{e\psi_p + G_1 - G_2}{\mathrm{k_B T}}\right). \quad \textbf{[S56]}$$

There exist multiple choices for the expressions k_{12} and k_{21}. For convenience and symmetry, we choose the following for the rate constants:

$$k_{12} = 10^{-\mathrm{pH_{periplasm}}} \exp\left(\alpha\left(\frac{e\psi_p + G_1 - G_2}{\mathrm{k_B T}}\right)\right), \quad \textbf{[S57]}$$

$$k_{21} = 10^{-\mathrm{pK_a^p}} \exp\left(-(1-\alpha)\left(\frac{e\psi_p + G_1 - G_2}{\mathrm{k_B T}}\right)\right). \quad \textbf{[S58]}$$

For symmetry, we have chosen $\alpha = 0.5$.

Electrostatic Steering

In this section, we provide more detailed calculations for our electrostatic steering hypothesis, as shown in the main text. We also provide support for the dipole approximation via comparison with an analogous calculation with point charges.

We note that, because no structure of the stator is yet available, the purpose of these calculations is quite qualitative. Our goal is to simply to predict what the electrostatic energy landscape should look like to support our steering hypothesis.

Dipole Approximation. As a first-order approximation, we consider the relevant charges on the FliG helix and the stator loops to be dipoles. We denote the rotor dipole moment as $\vec{p}_R^{\,k}$, where $k \in \{1 \ldots 26\}$ enumerates the number of FliGs on the rotor periphery. Likewise, the stator dipole moment is denoted as $\vec{p}_S^{\,i,N}$, where N enumerates the number of stator units, and i is the number of loops on a single stator. Here, for ease of exposition, we show electrostatic calculations for a single stator with a single loop ($i = 1$ and $N = 1$), but note that this calculation can be easily extended to the full stator model.

We calculate the electric field felt by the stator loop as

$$E = \sum_{k=1}^{26} E_k, \qquad \textbf{[S59]}$$

where

$$E_k = \frac{1}{4\pi\epsilon|r_k|^3}\left[3\left(\vec{p}_R^{\,k}\cdot\hat{r}_k\right)\hat{r}_k - \vec{p}_R^{\,k}\right]. \qquad \textbf{[S60]}$$

Here ϵ is relative permittivity of cytoplasm and $\vec{r}_k$ is a vector quantity that denotes the distance between the stator loop and the kth FliG.

From E_k, we calculate the interaction energy between the dipole on the stator loop $\vec{p}_S$ and the kth FliG $\vec{p}_R^{\,k}$ as

$$U_k = -\vec{p}_S \cdot E_k = \frac{1}{4\pi\epsilon|r_k|^3}\left[\left(\vec{p}_R^{\,k}\cdot\vec{p}_S\right) - 3\left(\vec{p}_R^{\,k}\cdot\hat{r}_k\right)\left(\vec{p}_S\cdot\hat{r}_k\right)\right]. \qquad \textbf{[S61]}$$

Similar to the calculation for total electric field, we have

$$U_{\text{stator}} = \sum_{k=1}^{26} U_k. \qquad \textbf{[S62]}$$

Note that, as the distance from the stator loop increases, the terms in the total electric field sum drop off as $1/|r^3|$, and so the contribution by FliGs located far from the stator loop is not appreciable.

To calculate the total energy in the system, we also add in the interaction energies between pairs of FliG molecules. However, we note that their relative positions do not change as the stator rotates, and so this consideration results simply in a translation of the entire landscape and has no effect on the topology.

$$U_{\text{total}} = U_{\text{stator}} + \sum_{i=1}^{26}\sum_{j=1,j\neq i}^{26}\frac{1}{4\pi\epsilon|r_{i,j}|^3}\left[\left(\vec{p}_R^{\,i}\cdot\vec{p}_R^{\,j}\right) - 3\left(\vec{p}_R^{\,i}\cdot\hat{r}_{i,j}\right)\left(\vec{p}_R^{\,j}\cdot\hat{r}_{i,j}\right)\right], \qquad \textbf{[S63]}$$

where $r_{i,j}$ is the displacement vector between the ith and jth FliG.

Comparison with Calculation Using Point Charges. We also performed the above calculations using point charges for the relevant residues on FliG and MotA loops. Because of the uncertainty in the position of the charges, we are interested primarily in a qualitative affirmation of our approximation—that is, the existence of a gently sloping, relatively wide energy well.

As in our dipole calculations, we consider the charged residues on the FliG to be positioned at π/4 to the horizontal (i.e., the charges are positioned along the dipole as shown in Fig. 2). Similarly, we position the charges on the stator loop along the dipole, positioned radially outward from the stator center. Given this configuration, we calculate the electrostatic energy as

$$U_{\text{pc}} = \underbrace{\sum_{i=1}^{8}\sum_{j=1,j\neq i}^{8}\frac{q_i q_j}{4\pi\epsilon|r_{i,j}|}e^{-|r_{i,j}|/\lambda_D}}_{\text{Interaction between stator charges}} + \underbrace{\sum_{i=1}^{52}\sum_{j=1,j\neq i}^{52}\frac{q_i q_j}{4\pi\epsilon|r_{i,j}|}e^{-|r_{i,j}|/\lambda_D}}_{\text{Interaction between stator charges}} + \underbrace{\sum_{i=1}^{8}\sum_{j=1}^{8}\frac{q_i q_j}{4\pi\epsilon|r_{i,j}|}e^{-|r_{i,j}|/\lambda_D}}_{\text{Interaction between charges on stator and FliGs}}. \qquad \textbf{[S64]}$$

We screen charges using a Debye length of $\lambda_D = 0.5$ nm. As before, $r_{i,j}$ denotes the displacement vector between charge i and charge j. Note that, similar to our dipole calculations, the first two terms of the energy are invariant to rotation of the stator. Therefore, they only serve to translate the entire energy landscape and do not affect the topology.

As shown in Fig. S7, the topology generated is indeed similar to that using the dipole approximation in the main text. The removal of certain charges may modify the energy landscape via a flattening or widening of the energy well. In conjugation with our electrostatic steering hypothesis, this may point to a possible explanation for experimental studies that show that mutation of charged residues reduces, but does not eliminate, motor function. Our methods can easily be extended using positional information from solved

structures to more quantitatively analyze the effects of these charges. Although such an investigation is certainly warranted, it is out of the scope of the current paper.

Centering the Stator. There is little structural information for the stator of the BFM. Therefore, in our calculations, we choose a possible position of the stator that is consistent with our model and experimental results. Firstly, we center the stator so that all four stator loops are able to access the FliG molecules. The occasionally observed backsteps imply that both pairs of loops must be able to execute a power stroke during motor function.

Preliminary calculations strongly suggest that the loop charges cannot be in plane with the charges on the FliG. The close proximity of the charges results in an electrostatic interaction far too strong to be feasible given the known efficiency of the BFM (i.e., far too much energy would be wasted in letting go). In-plane configurations that do not present both extremely steep and deep wells must place the stator out of reach of the FliGs.

Given these considerations, and noting that the stator and rotor have radii of respective lengths $\sim$ 20 nm and $\sim$ 2 nm, we center the stator at $(x_S, y_S, z_S) = (21, -2, 1)$ using a coordinate system with the rotor centered at the origin.

Ising Model to Describe Conformational Changes in FliG

The existence of motor backsteps in the absence of CheY-P has been largely attributed to microscopic reversibility. Given this constraint, there are three possibilities in explaining the backstep: (*i*) a backward transit of an ion from the cytoplasm to the periplasm; (*ii*) a sufficiently strained hook relaxes by moving the rotor backward; and (*iii*) a fluctuation that changes the orientation of FliG from its CCW to CW orientation.

The first two possibilities contradict our proposed model. For example, if the first case were correct, then a backstep would correspond to a reversal of the entire conformational change process. In this case, an ion bound to the Asp32 from the cytoplasm should restore the MotA helix from its bent state to the straight state in the presence of the ion. This is in direct contradiction to one of our model assumptions that MotA relaxes to the bent state due to the rearrangement in the hydrogen bonds caused by the binding of the ion to the Asp32 residue.

The second possibility (that the relaxation of an elastically strained hook due to several sequential forward steps leads to an occasional backstep) is also not feasible within the context of our model: A contact force guarantees that the rotor always follows the stator.

In this work, we attribute the molecular basis for the backstep to the third possible scenario: a conformational change in one (or more) individual FliGs on the periphery of the rotor. A FliG can exist in two states; in our model, these states correspond to two orientations of the FliG dipole vector. Our electrosteric model, in conjunction with an Ising model corresponding to the states of FliG, explains the existence of occasional backsteps in a self-consistent manner.

Briefly, a backstep results from a fluctuation of FliG from the CCW to the CW position. In this case, when the motor is predominantly moving in the CCW direction and whenever a FliG changes its state from CCW state to CW state and is close to a stator, then the stator—using MotA loops 2 and 4—applies the contact force and pushes the FliG in the backward direction.

Although the configuration of the FliGs in the CW orientation is fairly well agreed upon, the exact CCW configuration is still under debate. At least three possible orientations have been suggested, including directions orthogonal or 180° with respect to the CW orientation. Despite this uncertainty, it is generally believed that there are two significantly different orientations for each FliG.

As in other models, we describe the transitions between the two FliG orientations by a one-dimensional periodic Ising model consisting of 26 spins (corresponding to 26 FliGs). Each individual spin s_i can exist in two possible states corresponding to the two orientations of FliGs: $s_i = +1$ (CCW) and $s_i = -1$ (CW). The Hamiltonian is

$$H = -J \sum_{i,j=1}^{N} s_i s_j - h \sum_{i=1}^{N} s_i \qquad \textbf{[S65]}$$

where J denotes the nearest-neighbor pairwise interaction energy and h denotes the field biasing the FliGs to preferentially orient in a certain direction. Let $\{s_i\} = (s_1, s_2, s_3, \ldots, s_{26})$ denote a possible state of the rotor. The probability of such a state is given by the Boltzmann distribution $e^{-\beta H(\{s_i\})}/Z(J,H,\beta)$, where $Z(J,H,\beta)$ is the partition function. The partition function for a one-dimensional Ising model (Eq. **S65**) is obtained exactly using the transfer matrix approach and is given by

$$Z(J,h,\beta) = \lambda_+^N + \lambda_-^N \qquad \textbf{[S66]}$$

where

$$\lambda_\pm = e^{\beta J}\cosh(\beta h) \pm \sqrt{e^{2\beta J}\sinh^2(\beta h) + e^{-2\beta J}}. \qquad \textbf{[S67]}$$

To understand the backsteps while the motor is running predominantly in CCW direction, we calculate the probability that any FliG (or any spin) points in the CW direction. This is given by

$$p(s_i = -1) = \sum_{(s_1, \ldots, s_{i-1}, -1, s_{i+1}, \ldots, s_{26})} \frac{e^{-\beta H((s_1, \ldots, s_{i-1}, -1, s_{i+1}, \ldots, s_{26}))}}{Z} \qquad \textbf{[S68]}$$

where the summation is over all possible states fixing $s_i = -1$. In the following, we derive an analytical expression for the probability $p(s_i = -1)$.

Let us denote the probability for the spin $s_i = +1$ as $p(s_i = +1)$. Given the probabilities $p(s_i = +1)$ and $p(s_i = -1)$, the average value $\langle s_i \rangle$ of the spin s_i can be calculated as

$$\langle s_i \rangle = (1)p(s_i = +1) + (-1)p(s_i = -1) = 1 - 2p(s_i = -1). \quad \textbf{[S69]}$$

Moreover, the derivative of the partition function Z with respect to the field h yields

$$\frac{1}{N\beta Z}\frac{\partial Z}{\partial h} = \frac{1}{N}\sum_{\{s_i\}}\sum_i s_i \frac{e^{-\beta H(\{s_i\})}}{Z} = \langle s_i \rangle. \quad \textbf{[S70]}$$

Therefore, using Eqs. **S69** and **S70**, the probability that spin $s_i = -1$ can be obtained as

$$p(s_i = -1) = \frac{1 - \frac{1}{N\beta Z}\frac{\partial Z}{\partial h}}{2}. \quad \textbf{[S71]}$$

The derivative of the partition function with respect to the field h can be evaluated using the derivatives of the $\lambda_\pm$ functions, which are given by

$$\frac{\partial \lambda_\pm}{\partial h} = \beta \sinh(\beta h)\left(e^{\beta J} \pm \frac{e^{2\beta J}\cosh(\beta h)}{\sqrt{e^{2\beta J}\sinh^2(\beta h) + e^{-2\beta J}}}\right). \quad \textbf{[S72]}$$

Within the context of our model, the likelihood of a flip in FliG conformation corresponds directly to the likelihood of a backstep. That is, the probability that a FliG is in the CW state is given by Eq. **S71**. This is because the fundamental mechanics of a backstep is the same as that of a forward step; the difference between these two scenarios is wholly described by the difference in FliG configuration.

Suppose that the motor is moving primarily in the CCW direction. This means that the FliGs in close proximity to the stator loops are oriented to favor CCW rotation (that is, to favor interaction with MotA loops 1 and 3). However, if a FliG close to the stator is oriented to favor CW rotation, then the FliG interacts with MotA loops 2 and 4, resulting in a step in the CW direction (a backstep when the motor is moving primarily CCW). This probability is given by Eq. **S71**.

For the choice of the energy scale $\beta J = 2$ at room temperature and a biasing field of $\beta h = 0.05$, the probability that any FliG is in the CW state is $p(s_i = -1) = 0.08$. That is, on average, 8 out of every 100 torque-generating cycles will result in a backstep. Areas under the curve corresponding to forward and backward steps from data collected by Sowa et al. (16) indicate that $p(s_i = -1) \approx 0.073$ (Fig. S8).

The above analysis provides an explanation for how backsteps in the absence of CheY-P can arise from fluctuations in FliG configurations. However, it does not take into account how the above probabilities are affected by load or PMF. For example, the timescale of a single step depends on the load. If one assumes that this step is a backstep, then this particular FliG is pinned in the backwards orientation for the duration of that step. This CW defect in the FliG ring can affect the switching probabilities of the neighboring FliGs, resulting in further defects along the ring. Therefore, at higher loads, the probability of two (or more) subsequent backsteps may not be negligible. However, a complete understanding of the above requires a far more detailed analysis of an Ising model in conjunction with the proposed electrosteric model than is within the scope of this work.

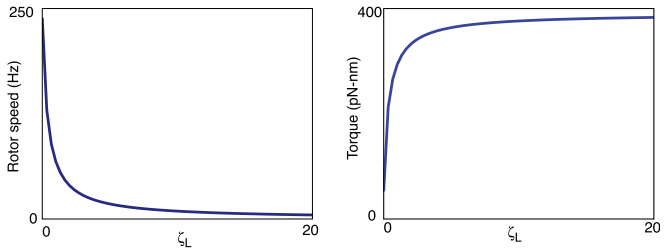

Fig. S1. (*A*) Rotor speed and (*B*) torque as a function of the load drag. ζ_L. Plotted from Eqs. **S26** and **S24**, respectively.

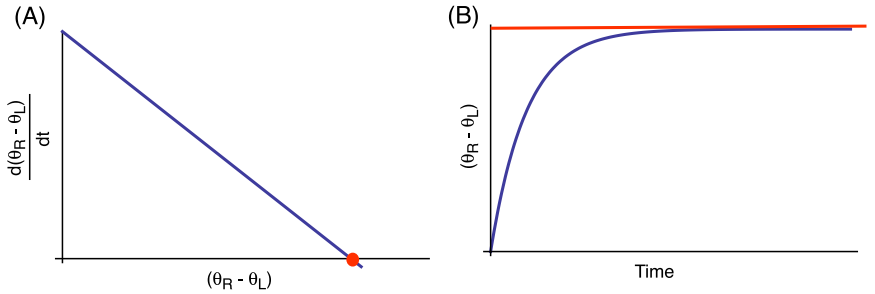

Fig. S2. Angular difference between rotor and load. (*A*) The change in $(\theta_R - \theta_L)$ with time decreases steadily until a fixed point is reached (marked in red). (*B*) Accordingly, $(\theta_R - \theta_L)$ increases and asymptotically reaches a steady state. The steady state is denoted by a red line, corresponding to the zero of $[d(\theta_R - \theta_L)]/dt$, shown as the red dot in *A*.

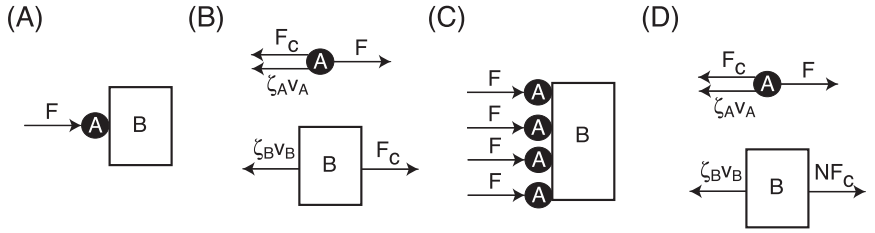

Fig. S3. Contact forces. (*A*) Case 1. A force *F* is applied to object *A*, which is in contact with object *B*. (*B*) Free-body diagrams for objects *A* and *B* arranged as in case 1. (*C*) Case 2. *N* objects of type *A* are in contact with object *B*, each with a force *F* applied to it. (*D*) Free-body diagrams for each object of type *A* as well as type *B* for case 2.

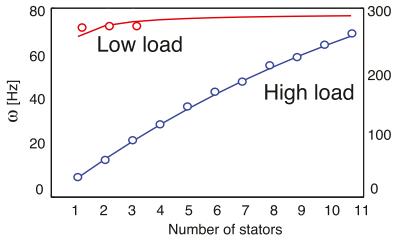

Fig. S4. Resurrection experiments at high and low load both show a nonlinear relationship between motor speed and stator number. Our model suggests that nonlinearities at high load may result from the nature of steric forces. Markers denote data from ref. 35; lines are model fits assuming synchronously stepping stators.

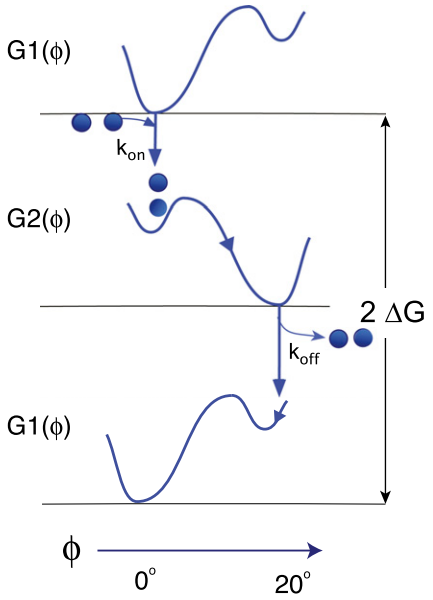

Fig. S5. A schematic of the stator potentials.

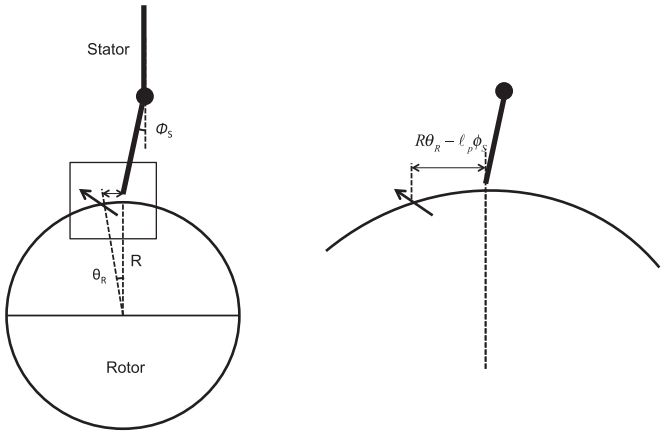

Fig. S6. A schematic of the geometry of rotor–stator contact during a half-step. The distance between the nearest FliG and the stator is then given by $x_{RS} = X_{RS} + R\theta_R - \ell_p\phi_S$. The contact force is zero whenever $x_{RS} \geq X_{RS}$. Moreover, the stator never is ahead of the rotor. This is ensured by choosing a time step such that the fluctuations from the random noise terms are small.

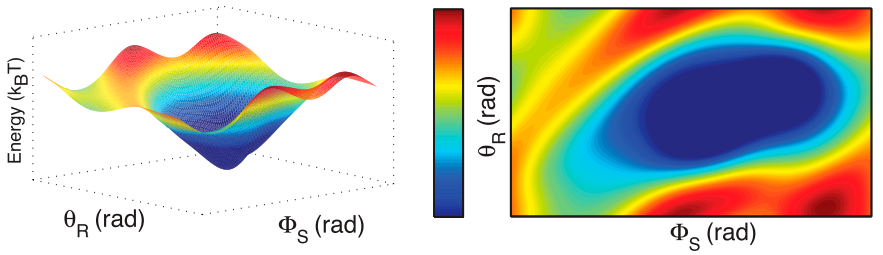

Fig. S7. Energy landscape during electrostatic steering calculated using point charges rather than dipoles. All parameters are defined as in the main text; the stator is centered at (21,-2,1), and the rotor is centered at the origin (all distances in nanometers).

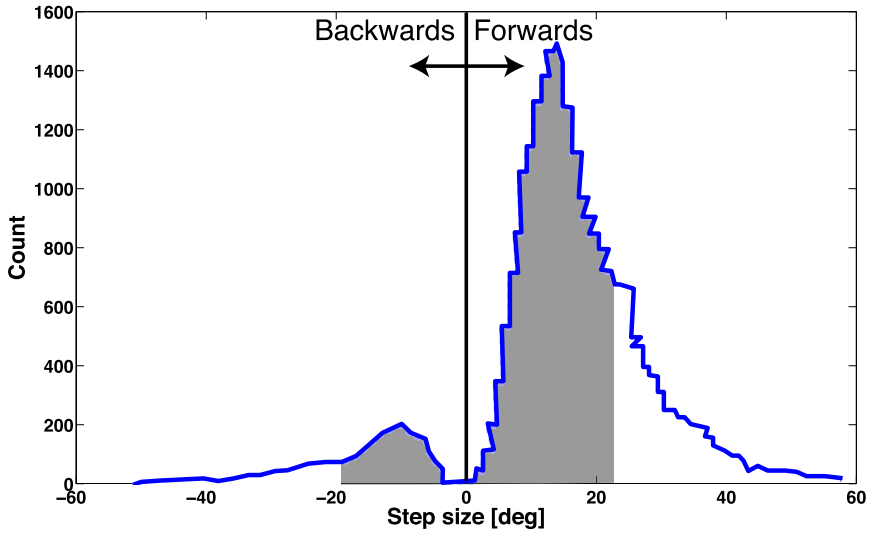

Fig. S8. Probabilities of backward steps relative to forward steps can be estimated using statistics from stepping experiments (data shown from ref. 16). The area under the curve for steps below and above 0° corresponds to forward and backward step probabilities, respectively. The areas on either side are calculated as highlighted in gray. Curves are truncated where each shows a second peak, corresponding to two steps being blurred together due to limitations in experimental resolution. The relative areas calculated for the data above suggest that the probability of a backward step is 7.3%.